Determination of mineral dissolution regimes using flow-through time-resolved analysis (FT-TRA) and numerical simulation

Bart De Baere[a,1], Sergi Molins[b], K. Ulrich Mayer[a], Roger François[a]

[a]*Department of Earth, Ocean and Atmospheric Sciences, University of British Columbia, 2020-2207 Main Mall, Vancouver, BC Canada V6T 1Z4*

[b]*Earth and Environmental Sciences, Lawrence Berkeley National Laboratory, One Cyclotron Rd, MS 74R316C, Berkeley CA 94720, USA*

ABSTRACT

Flow-through time resolved analysis (FT-TRA) involves subjecting small mineral samples (< 10 mg) inserted in a miniature flow-through cell (50 μL) to controlled flows of eluent analyzed on-line by ICP-MS. In this study, FT-TRA is used to empirically determine the dissolution regimes for the two well-studied minerals forsterite and calcite, representing minerals with relatively slow and fast dissolution kinetics. A proportional increase in steady-state effluent [Mg, Si] concentrations with increasing flow-through cell eluent residence times confirms a dominantly surface-controlled dissolution regime for a powdered forsterite sample at pH 2.3, implying that transport limitations are negligible. In contrast, the relationship between flow rates and dissolution rates for single grain calcite samples at pH 2.3 – 4 reveals that transport limitations affect the rate of calcite dissolution. To provide a quantitative and

[1]Corresponding author.
Email addresses: b.debaere@alumni.ubc.ca (B. De Baere), smolins@lbl.gov (S. Molins), rfrancoi@eos.ubc.ca (R. François), umayer@eos.ubc.ca (K.U. Mayer)

process-based assessment of the effect of diffusive transport limitations, simulations of the calcite experiments were performed with a high resolution, pore-scale model that considers the geometry of the calcite grain and the FT-TRA flow-through reactor. The pore-scale model reproduces the observed effluent [Ca] concentrations for all experimental conditions using a single set of surface kinetic parameters, by accounting for the formation of a diffusive boundary layer (DBL) that varies in thickness as a function of flow rates. These results demonstrate that combining FT-TRA with pore-scale modeling makes it possible to obtain unprecedented insights not achievable by either method separately, including quantification of DBL thicknesses and the determination of transport controls as a function of pH, flow velocity and residence times.

1. Introduction

1.1 Dissolution regimes

Accurately predicting mineral dissolution rates is essential for the investigation of many processes in environmental geochemistry, material science, and a wide range of related fields. One approach to reach this goal has been to measure mineral dissolution rates in laboratory experiments, from which dissolution rate parameters can be deduced and then used to predict rates of mineral dissolution under a wide range of conditions (e.g. White and Brantley, 1995). To obtain meaningful dissolution rate parameters that can be applied to a range of environmental conditions, experiments are normally designed to quantify surface-controlled dissolution rates, i.e. the intrinsic rate of detachment of dissolving species from the surface of the mineral (e.g. Berner, 1978; Compton and Unwin, 1990; Morse and Arvidson, 2002; Morse et al., 2007). However, rates measured in laboratory experiments may be affected by the hydrodynamic conditions under which the dissolution measurements were conducted (e.g. Sjöberg and Rickard, 1984), and thus may not be readily transposed to other conditions or compared between minerals and even mineral crystallographic surfaces.

When a mineral comes into contact with a fluid, a diffusive boundary layer (DBL) forms at the mineral-fluid interface, and dissolution occurs in two distinct steps: first the dissolving species must detach from the surface of the mineral, and second, they must diffuse through the DBL to the bulk solution (e.g. Morse and Arvidson, 2002). The slower of these steps controls the rate of mineral dissolution (e.g. Berner, 1978). When the dissolution rate is limited by the rate of detachment of dissolving species from the surface of the mineral, dissolution is "surface-controlled". When the dissolution rate of a mineral is limited by the rate of diffusion of dissolution products or reactants across the DBL, dissolution is "transport-controlled", often significantly limiting the progress of mineral dissolution at the mineral surface.

Under a surface-controlled dissolution regime and far-from-equilibrium conditions, rates of mineral dissolution can be described with rate laws of the form (e.g. Lasaga, 1998):

$$R_{surface} = \left(\frac{m}{m_0}\right)^{2/3} \sum_{i=1}^{N_p} k_i \, a_i^{n_i} \quad (1)$$

where $R_{surface}$ (moles m^{-2} s^{-1}) is the surface area normalized, surface-controlled dissolution rate, the $\left(\frac{m}{m_0}\right)^{2/3}$ term accounts for surface area loss over the course of a dissolution experiment, where the exponent $2/3$ is applicable for uniformly dissolving spheres or cubes (e.g. Appelo and Postma, 2005), N_p is the number of parallel reaction pathways, k_i (moles m^{-2} s^{-1}) is the dissolution rate constant for the i^{th} reaction pathway, a_i is the activity of the i^{th} species, and n_i is the reaction order of the i^{th} pathway.

Under a transport-controlled dissolution regime, the dissolving species build up in a diffusive boundary layer (DBL), and Fick's law dictates the rate of diffusion of products or reactants across the DBL (e.g. Lasaga, 1998):

$$R_{transport} = k_t \left(C_{surface} - C_{bulk}\right) \quad (2)$$

where $R_{transport}$ (moles m^{-2} s^{-1}) is the surface area normalized diffusion rate across the DBL, k_t (m s^{-1}) is the transport rate constant (with $k_t = D/\delta$, where D (m^2 s^{-1}) is the diffusion coefficient of the dissolved species, and δ (m) is the DBL thickness), $C_{surface}$ and C_{bulk} (moles m^{-3}) are the concentration of the dissolved species in contact with the surface of the mineral and in the bulk fluid, respectively.

1.2 Dissolution regimes as a continuum

In natural and engineered systems, evolving flow conditions may alter the balance between surface-controlled and transport-controlled dissolution kinetics. For a given mineral, the dissolution regime may shift from surface- to transport-controlled as the DBL increases in thickness, and vice versa, if the DBL thickness decreases. Similarly, under given hydrodynamic conditions, the dissolution regime may shift from surface- to transport-controlled as the rate of mineral dissolution increases.

When minerals dissolve, dissolution products detach from the surface and diffuse towards the bulk solution. It is important to note that at steady state, the rate of detachment must be equal to the rate of transport away from the mineral surface by diffusion. If the rate of detachment is slow, the transport rate is equally slow, and can be sustained with a small concentration gradient across the DBL. These conditions imply that the concentrations of dissolution products at the mineral surface are nearly equal to concentrations in the bulk solution. Under these conditions, the rate of dissolution is dominated by the detachment reaction at the mineral surface and is commonly referred to as surface-controlled. The relatively slow rate of detachment from the surface is not significantly affected by concentration build-up near the surface as a result of transport limitations. On the other hand, for minerals dissolving rapidly, the rate of transport must be equally rapid, which can require large concentration gradients across the DBL. Under these conditions, concentrations of dissolution products at the mineral surface tend to differ significantly from the corresponding concentrations in the bulk solution, in particular if

89 the DBL is relatively thick. DBL thickness is affected by hydrodynamic flow conditions at the pore
90 scale, with slower flow velocities resulting in a greater DBL thickness. In the extreme case, the
91 concentrations of dissolution products approach saturation at the mineral surface, driven by the need to
92 increase the diffusive flux away from the mineral surface. Under these conditions, transport limitations
93 result in a decrease in the detachment rate due to near-equilibrium conditions at the mineral surface,
94 and the dissolution rate of minerals is referred to as transport-controlled.

95 Notably, the two end-members described above (transport-controlled when $C_{surface} = C_{saturation}$;
96 surface-controlled when $C_{surface} = C_{bulk}$) can only be approached but never reached, otherwise
97 dissolution would stop. Instead, the dissolution rate is always controlled by a continuum between these
98 two extremes. In all steady-state mineral dissolution situations, the rate of detachment must be lower
99 than, but can be infinitesimally close to, its full potential, which is described by equation (1) with
100 activities of the bulk solution. This situation results in an essentially surface-controlled dissolution
101 regime. Likewise, the rate of transport cannot reach its full potential described by equation (2) for
102 $C_{surface} = C_{saturation}$ but can be infinitesimally close, resulting in an essentially transport-controlled
103 dissolution regime. Between these two extremes, both the detachment rate and the transport rate are
104 lower than their full potentials as the dissolution regime transits between surface- and transport-
105 controlled.

106 Describing a system as surface- or transport-controlled thus requires an arbitrary subdivision of
107 this continuum. Recently, Rimstidt (2015) proposed to make this distinction by using the diffusive
108 Damköhler number:

109 $$Da_{II} = R_{surface}/R_{transport} \quad (3)$$

110 where $R_{surface}$ is the rate of detachment at its full potential (as $C_{surface} \rightarrow C_{bulk}$) and $R_{transport}$ is the rate of
111 transport at its full potential (as $C_{surface} \rightarrow C_{saturation}$). When $R_{surface} > 10 \times R_{transport}$ (i.e. when rate

112 calculated with equation (1) > 10 x rate calculated from equation (2) with $C_{surface} = C_{saturation}$), the
113 dissolution regime is deemed surface-controlled, while $R_{surface} < 0.1\ R_{transport}$ indicates transport control.
114 Because the transition between the two regimes is gradual and the end-members are never truly
115 reached, an alternative to predicating arbitrary cut-offs would be to simply report the value of the
116 diffusive Damköhler number of the system to provide a sense of how far it is in one or the other regime
117 (i.e. large Da_{II} towards surface controlled vs small Da_{II} towards transport controlled), similar to the
118 approach proposed by Raines and Dewers (1997). However, in practice, the DBL thickness is often not
119 constant across the mineral surface, the gradient across the DBL is not linear due to the fact that flow
120 velocities gradually increase towards the bulk solution, and equilibrium concentrations for a given ion
121 ($C_{saturation}$) can also vary over the mineral surface. As a result, Damköhler numbers must vary over a
122 dissolving mineral surface and their calculation may be complex. Empirical determinations of
123 dissolution regime may thus provide a more practical approach.

124 1.3 The need to establish a dissolution regime

125 Because intrinsic mineral dissolution rate parameters must be measured under surface-controlled
126 conditions (e.g. Compton and Unwin, 1990), it is important to establish the dissolution regime under
127 which dissolution rates of minerals are measured before interpreting or using the results. Many of the
128 studies addressing mineral dissolution kinetics rely on measuring bulk solution concentrations to
129 estimate mineral dissolution rates (e.g. Plummer, 1978, 1979; Sjöberg, 1978; Sjöberg and Rickard,
130 1983, 1984). With the development of high-resolution imaging techniques such as Atomic Force
131 Microscopy (AFM) and Vertical Scanning Interferometry (VSI), some of the focus has now shifted
132 from bulk solution measurements to variations in nano-scale surface topography to estimate mineral
133 dissolution rates of the more soluble minerals (e.g. Liang and Baer, 1997; Arvidson et al, 2003; Ruiz-
134 Agudo and Putnis, 2012). Using this approach, dissolution rates are estimated from volume of mineral
135 loss to dissolution per unit time, converted into moles s^{-1} using the molar volume of the mineral.

Although this approach is fundamentally different from the methods using bulk solution composition, it also requires knowledge of the dissolution regime to interpret the data. Thus, a need exists to develop methodologies to determine the rate-limiting dissolution regime when measuring mineral dissolution rates, regardless of which technique is employed to quantify the surface-controlled mineral dissolution rates.

1.4 Previous approaches to determining dissolution regime

The need to determine the rate-limiting mineral dissolution step was quickly identified when studying the rate of dissolution of more soluble minerals such as calcite (e.g. Plummer et al., 1978, 1979; Sjöberg and Rickard, 1984; Murphy et al., 1989) or gypsum (e.g. Raines and Dewers, 1997a, 1997b; Jeschke et al., 2001). In principle, transport-controlled dissolution regimes can be identified when dissolution rates vary in response to changes in the thickness of the DBL. A commonly used approach involves measuring dissolution rates by dissolving fine-grained minerals and/or individual mineral crystals suspended in a stirred vessel. In this set up, controlling the thickness of the DBL is achieved by varying the stirring rate of the suspensions. Constant dissolution rates with varying stirring rates have been interpreted to indicate a surface-controlled dissolution regime (e.g. Sjöberg, 1978; Plummer et al., 1978; 1979; Busenberg and Plummer, 1986; Raines and Dewers, 1997b). However, Sjöberg and Rickard (1983) pointed out that such a system has poorly controlled hydrodynamics, and a lack of stirring dependence does not necessarily guarantee surface-controlled dissolution, but instead could indicate that, at some point, the effective thickness of the DBL does not change with stirring rate. This shortcoming led to the development of alternative approaches including the fluidized bed reactor, which produces a more even spatial distribution of suspended particles (e.g. Chou et al., 1989). The higher turbulence generated using this experimental design accelerates diffusional transport through the DBL, facilitating the establishment of surface-controlled dissolution conditions. However, it remains difficult to determine the actual dissolution regime with this experimental set up. Another widely used

approach relies on a rotating disc made of the mineral of interest, which is immersed in the reactive medium (e.g. Sjöberg and Rickard, 1983; 1984; Pokrovsky et al., 2005). Using this approach, assuming a laminar flow regime, the transport rate constant can be calculated with the solution of Levich (1962) based on a semi-infinite domain (Alkattan et al., 1998, Pokrovsky et al 2005):

$$k_t = 0.62\, D^{2/3}\, \nu^{-1/6}\, \omega^{1/2} \quad (4)$$

where ν is the kinematic viscosity of the solution and ω the disc rotation speed.

For mineral grains of arbitrary shape and size in finite reactor cells, however, solution of the flow, transport and reaction processes can only be achieved through numerical techniques. Recent advances in pore-scale modeling, involving the numerical solution of Navier – Stokes flow, advective-diffusive transport and dissolution equations, make it possible to capture transport limitations associated with reactive surfaces in more complex domain geometries without having to make any assumption about the thickness of the DBL (Molins et al., 2014; Molins, 2015). Although pore-scale numerical simulations provide a powerful means to elucidate transport limitations on mineral dissolution, these have not been performed in conjunction with experimental studies of dissolution regimes in single-crystal small-volume reactors.

1.5 Study Objectives

In this study, we build on the convergence of high-resolution experimental and numerical simulation techniques to study the mechanistic coupling between flow, transport and reactive processes at the micrometer scale. We do so by using FT-TRA experiments to empirically distinguish between surface- and transport-controlled dissolution regimes in combination with pore-scale modeling, which allows the quantitative interpretation of experimental data under various flow conditions. The combination of methods yields a novel and integrated experimental-modeling approach to study mineral dissolution kinetics.

2. Materials and methods

2.1 Sample origin, preparation and surface area measurement

Forsterite and calcite samples were obtained from Ward's Natural Science (items #49-1557 and #49-5860, respectively). Transparent forsterite grains ($Mg_{1.81}Fe_{0.18}Ni_{0.01}SiO_4$; Fo91) were handpicked, and ground down to a 63 – 150 µm size fraction. Pre-treatment was limited to ultrasonic cleaning with acetone until a clear supernatant was obtained. A subsample ($8.17 \times 10^{-3}\ g$) was dried-overnight in an oven at 60 ºC. The mineral grains were examined by scanning electron microscopy (SEM), which revealed that they were generally free of adhering fine particles (Fig. 1A). Specific surface area ($257.3\ cm^2\ g^{-1}$) was measured using multi-point BET (Brunauer et al., 1938) with N_2 adsorption using a Quantachrome Autosorb-1 surface area analyzer. Calcite mineral rhombs were individually picked, ultrasonically cleaned with acetone to remove fine particles adhering to the mineral surface, and oven-dried at 60 ºC (Fig. 1B). Geometric surface areas were estimated from images obtained with a Hitachi S-4700 field emission scanning electron microscope housed at the UBC BioImaging Facility. Individual calcite rhombs were positioned on a platform, and were manually repositioned to expose each rhomb face for a top-down field-of-view to allow for geometric surface area estimation.

2.2 FT-TRA module

Dissolution experiments were conducted using a flow-through module connected to an Agilent 7700x quadrupole ICP-MS housed at the Pacific Center for Isotopic and Geochemical Research (Fig. 2; De Baere, 2015; De Baere et al., 2015) to measure the release rate of Mg and Si to monitor forsterite dissolution and Ca to monitor calcite dissolution. The flow-through cell consisted of a 13mm diameter syringe filter (Millipore Inc. item #SLLGC13NL) mounted between two computer-controlled parallel solenoid valves (NResearch Inc. item#225T092C). This design provides 6 filter positions, allowing for efficient switching between blanks and samples, analyzed successively. Eluents were pumped from individual bottles (E1 – E4) with a Dionex ICS-3000 dual gradient pump that generates precise flow

rates covering 4 orders of magnitude ($0.16 \times 10^{-4} - 0.16\, mL\, s^{-1}$). With this experimental design, mineral dissolution rates can be measured over a wide range of eluent residence times within the flow-through cell ($V\ (0.05\, mL)/Q$). The pump was programmed with the Chromeleon® Chromatography Data System to control eluent composition for the experiment or standards for calibration. Another gradient pump was used isocratically in parallel, to continuously supply an internal standard (^{115}In) allowing for instrumental drift correction during time-resolved ICP-MS measurement. The eluent produced by the first pump either directly joined the internal standard stream (when running standards) or passed through the flow-through cell (when running samples) before merging with the internal standard stream. The flow rate of the internal standard was held constant ($1.66 \times 10^{-6}\, L\, s^{-1}$), while the flow generated by the other gradient pump was adjusted according to the experiment. ^{24}Mg, ^{28}Si, ^{44}Ca and ^{115}In were measured in time-resolved mode with helium to minimize isobaric interferences (McCurdy and Woods, 2004), and the ICP-MS output (cps) was corrected for dilution by the internal standard. Effluent [Mg, Si and Ca] concentrations were monitored in real time and experiments were terminated when steady-state release rates were observed. Forsterite and calcite dissolution rates were calculated by multiplying [Mg, Si; Ca] concentrations ($moles\, L^{-1}$) by the flow rate of the effluent ($L\, s^{-1}$). For forsterite, the Mg value ($moles\, s^{-1}$) was corrected for stoichiometry by dividing by 1.81, before dividing by the BET surface area associated with the weighed subsample to obtain a surface area normalized dissolution rate ($moles\, m^{-2}\, s^{-1}$). For calcite, the Ca value was divided by the geometric surface area exposed to the incoming eluent (5 faces of the calcite rhomb), obtained from SEM imagery, to obtain surface area normalized dissolution rates ($moles\, m^{-2} s^{-1}$).

2.3 Experimental design to establish dissolution regime

The purpose-built leaching module described above was used to empirically determine the dissolution regime from observing the evolution of mineral dissolution rates with eluent flow rate (Q). When mineral dissolution is close to the surface-controlled regime end member and experimental conditions

are maintained far-from-equilibrium (IAP $\ll K_{sp}$) in the FT-TRA module, the rate of mineral dissolution can essentially be described by equation (1) and dissolution rates should be quasi independent of DBL thickness, i.e., dissolution rates ($Q \times \mathrm{C}_{effluent}$) should remain nearly constant under varying flow rates (Fig. 3A under relatively fast flow rates). Under such mineral dissolution conditions, the steady-state concentration of dissolved species ($[\mathrm{effluent}]_{steady\ state}$) must increase nearly proportionally with eluent residence time ($cell\ volume\ (V)/Q$, Fig. 3B at relatively short eluent residence times). In contrast, if $[\mathrm{effluent}]_{steady\ state}$ deviates strongly from linearity with residence time (Fig. 3B at relatively long eluent residence times), dissolution rates are affected by diffusive transport limitations through the DBL (Fig. 3A under relatively slow flow rates). The ability to observe transport limitations stems from the increase in thickness of the DBL as flow rate decreases and residence time increases (equation 2). As a result, $C_{surface}$ gradually increases from C_{bulk}, when the DBL is sufficiently thin, towards saturation as the DBL widens.

To test this hypothesis, weighed forsterite powders or individual calcite rhombs were placed in the flow-through cell and exposed to incoming effluents of constant pH (2.3, 3.3 and 4.0) over a range of flow rates spanning three orders of magnitude ($1.67 \times 10^{-7} - 1.25 \times 10^{-4} L\ s^{-1}$). Dissolution was carried out until a steady-state eluent concentration was reached (monitored by online ICP-MS time-resolved analysis). An overview of experiments conducted is provided in Table 1. A range in analytical grade (Seastar™) HNO_3 concentrations was used to generate acidic eluents at pH 2.3, 3.3 and 4.0. Experiments were carried out at room temperature.

2.4 Rate equations

The forsterite dissolution rate equation (equation 5) was derived from equation (1). Because the experiments were carried out under acidic and far-from-equilibrium conditions, it was sufficient to solely consider the H^+ reaction pathway (e.g. Rimstidt et al., 2012):

$$R_{surface} = k_{H^+}(a_{H^+})^{0.5} \quad (5)$$

A constant surface area was assumed in the forsterite dissolution experiments, given the limited amount of sample loss (< 1%, calculated using integrated $[Mg, Si]_{effluent}$ concentrations), allowing the term $\left(\frac{m}{m_0}\right)^{2/3}$ to be omitted.

The calcite dissolution rate equation (equation 6) used for data interpretation in the pore-scale model was also derived from equation (1).

$$R_{surface} = (k_1 a_{H^+} + k_2 a_{CO_2} + k_3 a_{H_2O})(1 - IAP/K_{sp}) \quad (6)$$

The faster reaction kinetics of calcite required this rate expression to be expanded by combining kinetic and thermodynamic concepts considering both the forward and backward reactions (i.e. ion detachment and reattachment). The inclusion of the thermodynamic affinity term $(1 - IAP/K_{sp})$, where IAP/K_{sp} is the ratio of the ion activity product at the mineral surface (IAP) to the solubility product of the mineral (K_{sp}), ensures that modeled dissolution rates decrease if equilibrium conditions are approached at the mineral surface. Similar to the forsterite dissolution experiments, a constant surface area was assumed, justified by sample losses limited to < 1% for all experiments (calculated using integrated $[Ca]_{effluent}$ concentrations).

2.5 Pore-scale modeling

To delineate transport-controlled processes occurring during calcite dissolution under varying incoming eluent velocities, high-resolution pore-scale simulations were performed using the approach of Molins

et al. (2012, 2014). A 3-dimensional domain was constructed consisting of a cylinder (0.4 cm in diameter and 0.4 cm in length) at the bottom of which a cubic calcite grain rested, representing the FT-TRA calcite dissolution experimental design (3-dimensional model domain shown in Fig. 4). Simulations were run at a 62.5 μm resolution. The dimensions of the grains were varied in each simulation such that their surface areas were consistent with the measured geometric surface area obtained from SEM imagery for each experiment. This approach resulted in slightly different grain sizes in each simulation. Fluid flow was obtained by solving the incompressible Navier–Stokes equations in the cell space (Molins et al., 2012), with the eluent solution entering the reactor in the space between the grain and the walls of the cylinder. Transport of 4 aqueous components ($H^+, CO_{2(aq)}, Ca^{2+}, NO_3^-$) was simulated with the advection-diffusion equation. The reactive components involved 8 aqueous equilibrium complexation reactions (Table 2). The rate of calcite dissolution was calculated directly at the mineral surface. Solid−fluid interfaces were represented explicitly as embedded boundaries within each of the grid cells of the structured mesh (Molins et al. 2012). In this approach, the solid-fluid interfaces intersect the grid cells rather than follow their boundaries. The governing equations are then solved with a finite volume method which accurately accounts for the volumes occupied by both fluid and solid and for the interfacial area between fluid and solid. The rate constants k_1 ($0.89\ moles\ m^{-2}\ s^{-1}$), k_2($5.01\ \times\ 10^{-4}\ moles\ m^{-2}\ s^{-1}$) were sourced from Chou et al. (1989) and k_3 ($2.34\ \times\ 10^{-6}\ moles\ m^{-2}\ s^{-1}$) was sourced from Busenberg and Plummer (1986). The use of these published rate constants in combination with measured surface areas without any further calibration was intended to evaluate whether a process-based pore-scale model that accounts for transport limitations can reproduce the experimental data. Because the dissolution rate is calculated at the mineral surface by the pore-scale model, rate constants used in the model are free of transport limitations, and must be taken constant for all flow velocities and pH conditions. Diffusive

boundary layer thickness and resulting transport-controlled dissolution rates are not specified, but are quantified from the simulation results.

3. Results and Discussion

3.1 Forsterite

Steady-state effluent [Mg, Si] concentrations were achieved within an hour (Fig. 5C) at eluent pH 2.3 and concentrations were found to increase proportionally with eluent residence time (Fig. 5A, 5B), following expectations for a dissolution reaction that is overwhelmingly surface-controlled for all eluent flow rates used. Experimentally derived forsterite dissolution rates vary within ± 0.21 log units across all flow rates (error = 2σ, as shown in Fig. 5D), which is a typical range for dissolution rates determined within a single laboratory (e.g. Brantley, 2008: p.175). This variability is greater than expected from analytical uncertainties, confirming previous observations (e.g. Brantley, 2008; Rimstidt et al., 2012) and likely reflects variability in the number and distribution of reactive sites, as dissolution proceeds (e.g. Lüttge et al., 2013). The dissolution rates measured at all flow rates ($2.53 \pm 0.59 \times 10^{-9}\, moles\, m^{-2}\, s^{-1}$) at pH 2.3 yield a dissolution rate constant ($2.53 \pm 0.59 \times 10^{-9}/(10^{-2.3})^{0.5} = 0.36 \pm 0.08 \times 10^{-7} moles\, m^{-2}\, s^{-1}$) consistent with published values (De Baere et al., 2015 and references therein). As the forsterite dissolution regime is widely recognized to be surface-controlled under acidic conditions (e.g. Pokrovsky and Schott, 2000), our findings illustrate how our experimental set up can empirically confirm the presence of a dissolution regime dominated by surface-control. Under these conditions, a modeling analysis to quantify transport limitation is not necessary, because experimental results are able to demonstrate conclusively the predominantly surface-controlled nature of the dissolution of powdered forsterite samples.

322 3.2 Calcite

323 3.2.1 Experimental results

324 Similar to the forsterite experiment, steady-state Ca concentrations ($[Ca]_{steady\ state}$) were achieved within
325 an hour at all flow rate conditions (Fig. 6D). However, for calcite dissolution it is evident that $[Ca]_{effluent}$
326 is not a linear function of residence time (Figs. 6A, 6B, 6C), indicating that dissolution is affected by
327 transport limitations. Calcite dissolution rates calculated by multiplying averaged $[Ca]_{steady\ state}$ by flow
328 rates at pH 2.3, 3.3 and 4.0 increase with decreasing pH and with increasing flow (shown in Figs. 7A,
329 7B and 7C respectively). The experimental data show a quasi linear dependence of the logarithm of the
330 dissolution rate on the logarithm of the flow rate (Fig. 7A, B and C). A linear fit to these data ($\log r = n + m \log Q$) yields m = 0.513 (R = 0.992) for pH 2.3, m = 0.502 (R = 0.986) for pH 3.3, and m =
332 0.308 (R = 0.986) for pH 4.0. At pH 2.3 and 3.3, the approximately square-root dependence ($m \approx 0.5$)
333 on the flow rate found here is comparable to the square-root dependence on the rotation speed of the
334 rotating disc solution of Levich (1962, Eq. 4). Deviations from linearity at pH 4.0 for low flow rates
335 (<0.05 x 10^{-3} L s^{-1} or Log Q < -1.3, hypothetical linear fit using $m = 0.5$ illustrated in Fig. 7C) likely
336 indicate a transition away from the transport-controlled dissolution regime ($m = 0.5$) towards a
337 surface-controlled regime ($m = 0$), and heavily weigh the fit towards a value of m smaller than at pH
338 2.3 and pH 3.3 (0.308, dashed line in Fig. 7C).

339 3.2.2 Pore-scale modeling analysis

340 Using a single set of dissolution rate constants, the pore-scale model was able to reproduce these
341 experimental data reasonably well, particularly at pH 2.3 and 3.3, where the departure of linearity at
342 decreasing flow rates was not observed (Fig. 7A, B and C). Based on the agreement with effluent
343 experimental data, the modeling results support the interpretation of FT-TRA experimental data that
344 calcite dissolution rates are strongly affected by transport limitations under these conditions.

345 The pore-scale model also revealed the presence of a nearly stagnant fluid pocket on the lee side
346 of the calcite rhomb, where reaction products build up and pH increases (Fig. 8). In fact, at this surface,

the thermodynamic affinity term in equation (6) departs significantly from unity in some of the simulations due to slow flow conditions. As a result, dissolution rates at this surface were much slower and contributed little to the overall calcite dissolution rate. In contrast, dissolution rates from the four calcite surfaces parallel to the mean flow direction are faster due to the smaller thickness of the DBL and more rapid solute exchange with the bypassing fluid. Figure 8 also clearly shows that pH at the mineral surfaces parallel to the direction of flow deviates to various degrees from eluent and bulk solution pH, resulting in different levels of transport limitations for calcite dissolution as a function of flow rate and eluent pH. A closer examination of the model results shows that the simulated thickness of the DBL increases with decreasing flow rates, with a strong effect on pH at the mineral surface, which in turn progressively limits mineral dissolution rates (Fig. 9). The deviations of pH within the DBL from bulk solution pH can be taken as a direct proxy for the effect of transport limitations on dissolution rates at the surface (equation 6) and demonstrate that transport limitations play a role for all experimental conditions considered.

Despite the observed changes of surface pH the numerical simulations for pH 2.3 and 3.3 show that the concentrations in the solution immediately adjacent to the mineral surface remain such that the $k_1 a_{H^+}$ term of Eq. (6) continues to dominate the intrinsic surface rate. This is also the case at pH 4.0 and fast flow rates; however, at pH 4.0 and slow flow rates, the pH at the surface increases to circum-neutral and even slightly alkaline values, further inhibiting mineral dissolution. The simulation shows that in this transition, the shift of pH pushes the rate into a regime where the controlling mechanism is the cation hydration-hydrolysis step rather than the stepwise proton-promoted mineral dissolution (Eq. 6). In this sense, the simulations also demonstrate how transport limitations can lead to a shift of the dissolution mechanism.

In Fig. 10, the simulated thicknesses of the DBL extracted from the plots in Fig. 9 are plotted against the flow rate, showing the decrease in thickness with increasing flow rate. By analogy between Q and ω from the Levich (1962) rotating disc solution, we assumed a relationship of the form $\delta =$

372 kQ^{-m} to capture the dependence of the DBL thickness on flow rates observed in simulation results
373 (Fig. 9). For this purpose, we used the value of m obtained in the earlier linear fits to experimental data
374 (Fig. 7). The fit to the simulated DBL thicknesses is remarkably good except at the fastest flow rates.
375 At fast flow rates, the DBL shrinks significantly and the discretization used for the simulations is not
376 fully sufficient; i.e. the DBL is captured within only one or two grid cells (Fig. 10). This limitation
377 likely leads to an underestimation of transport limitations and as a result to an overestimation of the
378 effective rates.
379
380 3.3 Added value of FT-TRA and pore-scale modeling
381 Our approach combines laboratory experiments and numerical simulations to gain insight into the
382 dissolution regimes over a range of flow conditions, which is a unique contribution of this work. Other
383 approaches have tackled this issue with either exclusively experimental methods (e.g. Erga and
384 Terjesen, 1956; Sjöberg, 1976; Plummer et al., 1978; Sjöberg and Rickard, 1984; Colombani, 2008), or
385 with experimental methods combined with simple mathematical solutions (e.g. Alkattan et al., 1998,
386 Pokrovsky et al., 2005), as well as exclusively mathematical methods (e.g. based on the film theory:
387 Rimstidt, 2015).
388 In terms of the experimental contribution, FT-TRA is a new approach when applied to study the
389 dissolution kinetics of minerals. The present study demonstrates that FT-TRA is suitable for
390 empirically establishing the dissolution regime, and when combined with pore-scale modeling FT-TRA
391 provides detailed insights into transport limitations. Combining FT-TRA with numerical simulations is
392 facilitated by the low detection limits of ICP-MS, which allows dissolution of single crystals (and
393 potentially single mineral cleavage surfaces) in small reaction cells of simple geometry. The small
394 volume of the reaction cell also reduces the time needed to reach steady-state dissolution, which in
395 conventional larger mixed flow reactors is primarily dictated by the residence time of the eluent in the
396 reactor (De Baere et al., 2015). This characteristic of the experimental set up used in this study also

facilitates efficient duplication of dissolution experiments and statistical analysis of the results to assess the underlying causes for the large variability observed in dissolution rates measured in laboratories (e.g. Rimstidt et al., 2012). Although not directly relevant to the present study, the high temporal resolution afforded by FT-TRA also provides detailed information on the evolution of dissolution rates and stoichiometries when minerals are subjected to abrupt or transient dissolution episodes, documenting in particular the gradual formation of surface leached layers in unprecedented detail and identifying sporadic and abrupt exfoliation events (De Baere et al., 2015).

As for the modeling contribution, we could show that direct numerical simulation can be a very powerful addition to the study of conditions in single-crystal small-volume reactors. In this paper, we have limited ourselves to assuming simple cubic grain geometry and that all surfaces of the mineral have homogeneous reactivity. However, this is not a requirement. The modeling approach also allows resolution of complex geometries at very high resolution, which can be incorporated in the model from microtomographic images (Molins et al., 2014) or from FIB-SEM characterization (Trebotich and Graves, 2015). In addition, recent studies have explored differences of surface-dominated rates on different surfaces of the same mineral (Fischer et al., 2012). One can envision the current model to incorporate this heterogeneous reactivity by tagging specific regions of the mineral surfaces differently. Further, the model could explore the effect of the orientation of the grain orientation to the flow direction in the reactor, as in Godinho et al. (2014). The evolution of the surfaces due to dissolution, where the shape of the crystals changes with time, is a subject of interest as well and currently mathematical techniques such as those proposed by Miller and Trebotich (2012) are being implemented in the model to capture this evolution. In porous materials, this would make it possible to capture e.g. the differential evolution of pores and pore throats.

4. Conclusions and future research direction

This study demonstrates that FT-TRA can be used to empirically establish mineral dissolution regimes. We demonstrated how FT-TRA can be used to identify predominantly surface-controlled dissolution using forsterite. In contrast, applying FT-TRA to calcite dissolution demonstrated how predominantly transport-controlled dissolution can be identified. The ability to combine FT-TRA measurements with 3-dimensional pore-scale modeling provides unprecedented insights into the transport and reactive processes taking place in the flow-through reactor. This study demonstrates that the pore-scale model is able to accurately capture hydrodynamic effects and transport limitations on mineral dissolution using a single set of surface-controlled rate parameters for a range of pH and flow conditions. As a result, pore-scale model parameter optimization will allow the estimation of mineral dissolution parameters, even when experimental conditions are inadequate to produce predominantly surface-controlled dissolution conditions. Future work should include developing different flow-through cell designs to allow higher resolution pore-scale modeling, and measuring additional effluent parameters (e.g. pH) to better constrain modeling results and provide additional means to estimate dissolution rate parameters.

The ability to experimentally validate reactive transport modeling is also of particular interest to a wide variety of research areas, including the problems of scaling (e.g. Li et al., 2008) and optimizing CO_2 injection methodology for carbon sequestration (e.g. Trebotich et al., 2014). For example, using the pore-scale modeling tools used in this study, small scale fluid-solid interfaces can be resolved to achieve a mechanistic understanding on how to control CO_2 injection in the subsurface (op. cit.).

Finally, beyond the establishment of 'classical' dissolution rate constants, future work should also explore the possibility of incorporating AFM or VSI as part of a FT-TRA experiment to couple surface micro-topography observations and high resolution bulk solution concentration measurements to link the evolution of reactive surface sites to dissolution rates, and address (1) the long-standing problem of surface normalization (e.g. Lüttge et al., 2005 and references therein) and (2) the ongoing

443 debate concerning the validity of using single rate constants to describe mineral dissolution (e.g. Lüttge
444 et al., 2013; Fischer et al., 2012, 2014, 2015).

445 The multi-faceted applications and encouraging results obtained in this study and a companion
446 paper (De Baere et al., 2015) warrants further development of FT-TRA for mineral dissolution kinetics
447 studies (De Baere, 2015).

448 ## Acknowledgements

449 The authors would like to thank 3 anonymous reviewers for constructive criticisms and feedback. S.M.
450 was supported as part of the Center for Nanoscale Control of Geologic CO_2, an Energy Frontier
451 Research Center funded by the U.S. Department of Energy, Office of Science, Office of Basic Energy
452 Sciences under Award Number DE-AC02-05CH11231. The authors would like to acknowledge Vivian
453 Lai and Marghaleray Amini at the Pacific Centre for Isotopic and Geochemical Research (PCIGR).
454 Method development has been made possible using a NSERC Research Tools and Instrumentation
455 grant. Finally, BDB thanks Derrick Horne for technical SEM assistance and training at the UBC
456 BioImaging Facility.

457 ## References cited

458 Alkattan, M., Oelkers, E.H., Dandurand, J.-L., Schott, J., 1998. An experimental study of calcite and
459 limestone dissolution rates as a function of pH from 1 to 3 and temperature from 25 to 80ºC.
460 Chem. Geol. 151, 199– 214.

461 Arvidson, R.S., Ertan, I.E., Amonette, J.E., Lüttge, A., 2003. Variation in calcite dissolution rates: A
462 fundamental problem? Geochim. Cosmochim. Acta 67, 1623–1634.

463 Appelo, C.A.J., Postma, D., 2005. Geochemistry, groundwater and pollution, 2nd edition. A.A. Balkema
464 Publishers, Leiden, The Netherlands.

465 Berner, R.A., 1978. Rate control of mineral dissolution under earth surface conditions. Am. J. Sci. 278,

1235–1252.

Brantley S.L., 2008. Kinetics of Mineral Dissolution, in: Brantley S.L., Kubicki J.D., White A.F. (Eds.), Kinetics of Water-Rock Interaction, Springer Science, New York, pp. 151–210.

Busenberg E., Plummer L.N., 1986. Studies in Diagenesis. U.S. Geol. Surv. Bull. 1578, 139–168.

Brunauer S., Emmett P.H., Teller E. (1938) Adsorption of Gases in Multimolecular Layers. J. Am. Chem. Soc. 60, 309–319.

Casey, W.H., 1987. Heterogeneous kinetics and diffusion boundary layers: the example of reaction in a fracture. J. Geophys. Res. 92, 8007-8013.

Chou L., Garrels R., Wollast R., 1989. Comparative-Study of the Kinetics and Mechanisms of Dissolution of Carbonate Minerals. Chem. Geol. 78, 269–282.

Colombani, J., 2008. Measurement of the pure dissolution rate constant of a mineral in water. Geochim. Cosmochim. Acta 72, 5634-5640.

Compton R.G., Unwin P.R., 1990. The Dissolution of Calcite in Aqueous Solution at pH < 4: Kinetics and Mechanism. Philos. Tr. R. Soc. S-A 330, 1–45.

De Baere, B., François, R., Mayer, K.U., 2015. Measuring mineral dissolution kinetics using on-line flow-through time resolved analysis (FT-TRA): an exploratory study using forsterite. Chem. Geol. 413, 107-118.

De Baere, B., 2015. Investigating mineral dissolution kinetics by flow-through time-resolved analysis (FT-TRA). Ph.D. thesis, University of British Columbia, http://hdl.handle.net/2429/55737

De Giudici, G., 2002. Surface control vs. diffusion control during calcite dissolution: dependence of step-edge velocity upon solution pH. Am. Mineral. 87, 1279-1285.

Duckworth, O.W., Martin, S.T., 2003. Connections between surface complexation and geometric models of mineral dissolution investigated for rhodochrosite. Geochim. Cosmochim. Acta 67, 1787–1801.

490 Erga, O., Terjesen, S.G., 1956. Kinetics of the heterogeneous reaction of calcium bicarbonate formation
491 with special reference to copper ion inhibition. Acta Chem. Scand. 10, 872-874.
492 Fischer, C., Arvidson, R.S., Lüttge, A., 2012. How predictable are dissolution rates of crystalline
493 material? Geochim. Cosmochim. Acta 98, 177-185.
494 Fischer C., Kurganskaya I., Schäfer T., Lüttge A., 2014. Variability of crystal surface reactivity: What
495 do we know? Appl. Geochem. 43, 132–157.
496 Fischer, C., Finkeldei, S., Brandt, F., Bosbach, D., Lüttge, A., 2015. Direct measurement of surface
497 dissolution rates in potential nuclear waste forms: the example of pyrochlore. Appl. Mater.
498 Interfaces 7, 17857-17865.
499 Godinho, J. R. A., Piazolo, S., Evans, L., 2014. Simulation of surface dynamics during dissolution as a
500 function of the surface orientation: Implications for non-constant dissolution rates, Earth Planet.
501 Sc. Lett., 408, 163–170, doi:10.1016/j.epsl.2014.10.018.
502 Jeschke, A.A., Vosbeck, K., Dreybrodt, W., 2001. Surface controlled dissolution rates of gypsum in
503 aqueous solutions exhibit nonlinear dissolution kinetics. Geochim. Cosmochim. Acta 65, 27-34.
504 Lasaga, A.C., 1998. Kinetic Theory in the Earth Sciences. Princeton University Press, Princeton, New
505 Jersey.
506 Levich, V. G. , 1962. Physicochemical Hydrodynamics. Prentice-Hall. Englewood Cliffs, New Jersey.
507 Liang Y., Baer D.R., 1997. Anisotropic dissolution at the $CaCO_3$ – water interface. Surf. Sci. 373, 275–
508 287.
509 Li, L., Steefel, C.I., Yang, L., 2008. Scale dependence of mineral dissolution rates within single pores
510 and fractures. Geochim. Cosmochim. Acta 72, 360-377.
511 Lüttge, A., 2005. Etch pit coalescence, surface area, and overall mineral dissolution rates. Am. Mineral.
512 90, 1776-1783.
513 Lüttge, A., Arvidson, R.S., Fischer, C., 2013. A stochastic treatment of crystal dissolution kinetics.

514 Elements 9, 183-188.
515 McCurdy E., Woods G., 2004. The application of collision/reaction cell inductively coupled plasma
516 mass spectrometry to multi-element analysis in variable sample matrices, using He as a non-
517 reactive gas. J. Anal. At. Spectrom. 19, 607-615.
518 Miller, G., Trebotich, D., 2012. An embedded boundary method for the Navier–Stokes equations on a
519 time-dependent domain, Commun. Appl. Math. Comput. Sc., 7(1), 1–31,
520 doi:10.2140/camcos.2012.7.1.
521 Molins S., Trebotich D., Steefel C.I., Shen C., 2012. An investigation of the effect of pore scale flow
522 on average geochemical reaction rates using direct numerical simulation. Water Resour. Res. 48,
523 1–11.
524 Molins S., Trebotich D., Yang L., Ajo-Franklin J.B., Ligocki T.J., Shen C., Steefel C.I., 2014. Pore-
525 Scale Controls on Calcite Dissolution Rates from Flow-through Laboratory and Numerical
526 Experiments. Environ. Sci. Technol. 48, 7453–7460.
527 Molins, S., 2015. Reactive interfaces in direct numerical simulation of pre-scale processes. In: (Eds:
528 Steefel, C.I., Emmanuel, S., Anovitz, L.M.) Pore-scale geochemical processes. Rev. Mineral.
529 Geochem. 80, 461-481.
530 Morse J.W. and Arvidson R.S., 2002. The dissolution kinetics of major sedimentary carbonate
531 minerals. Earth Sci. Rev. 58, 51–84.
532 Morse, J.W., Arvidson, R.S., Lüttge, A., 2007. Calcium Carbonate Formation and Dissolution. Chem.
533 Rev. 107, 342–381.
534 Murphy, W.M., Oelkers, E.H., Lichtner, P.C., 1989. Surface reaction versus diffusion control of
535 mineral dissolution and growth rates in geochemical processes. Chem. Geol. 78, 357–380.
536 Pleskov Y.V., Filinovskii V.Y., 1976. The rotating disc electrode. Consultants Bureau - New York.

Plummer L.N., Wigley T., Parkhurst D.L., 1978. The kinetics of calcite dissolution in CO_2-water systems at 5 to 60 degrees C and 0.0 to 1.0 ATM CO_2. Am. J. Sci. 278, 179–216.

Plummer L.N., Pakhurst D., Wigley T.M.L., 1979. Critical review of the kinetics of calcite dissolution and precipitation, in: Jenne, E.A. (Ed.) Chemical Modeling in Aqueous Systems, American Chemical Society Volume 93, pp. 537–573.

Pokrovsky, O.S. and Schott, J., 2000. Kinetics and mechanism of forsterite dissolution at 25°C and pH from 1 to 12. Geochim. Cosmochim. Acta 64, 3313–3325.

Pokrovsky O.S., Golubev S.V., Schott J., 2005. Dissolution kinetics of calcite, dolomite and magnesite at 25 ºC and 0 to 50 atm pCO_2. Chem. Geol. 217, 239–255.

Raines, M.A., Dewers, T.A., 1997a. "Mixed" kinetics control of fluid-rock interaction in reservoir production scenarios. J. Petrol. Sci. Eng. 17, 139-155.

Raines, M.A., Dewers, T.A., 1997b. Mixed transport/reaction control of gypsum dissolution kinetics in aqueous solutions and initiation of gypsum karst. Chem. Geol. 140, 29-48.

Rickard D., Sjöberg E.L., 1983. Mixed control of calcite dissolution rates. Am. J. Sci. 283: 815–830.

Rimstidt, J.D., Brantley, S.L., Olsen, A.A., 2012. Systematic review of forsterite dissolution rate data. Geochim. Cosmochim. Acta 99, 159–178.

Rimstidt, J.D., 2015. Diffusion control of quartz and forsterite dissolution rates. Appl. Geochem. 61, 99-108.

Ruiz-Agudo, E., Putnis, C.V., 2012. Direct observations of mineral-fluid reactions using atomic force microscopy: the specific example of calcite. Mineral. Mag. 76, 227–253.

Salehikhoo, F., Li, L., Brantley, S.L., 2013. Magnesite dissolution rates at different spatial scales: The role of mineral spatial distribution and flow velocity. Geochim. Cosmochim. Acta 108, 91-106.

559 Sjöberg, E.L., 1976. A fundamental equation for calcite dissolution kinetics. Geochim. Cosmochim.
560 Acta 40, 441-447.

561 Sjöberg E.L., Rickard D.T., 1983. The influence of experimental design on the rate of calcite
562 dissolution. Geochim. Cosmochim. Acta 47, 2281–2285.

563 Sjöberg E.L., Rickard D.T., 1984. Calcite dissolution kinetics: surface speciation and the origin of the
564 variable pH dependence. Chem. Geol. 42, 119–136.

565 Sjöberg E.L., 1978. Kinetics and mechanisms of calcite dissolution in aqueous solutions at low
566 temperatures. Stockh. Contrib. Geol. 32, 1–94.

567 Steefel, C.I., Appelo, C.A.J., Arora, B., Jacques, D., Kalbacher, T., Kolditz, O., Lagneau, V., Lichtner,
568 P.C., Mayer, K.U., Meeussen, J.C.L., Molins, S., Moulton, D., Parkhurst, D.L., Shao, H.,
569 Šimůnek, J., Spycher, N., Yabusaki, S.B., Yeh, G.T., 2015. Reactive Transport Codes for
570 Subsurface Environmental Simulation, Comput. Geosci. 19, 445–478, doi: 10.1007/s10596-014-
571 9443-x

572 Trebotich, D., Adams, M.F., Molins, S., Steefel, C.I., Shen, C., 2014. High-resolution simulation of
573 pore-scale reactice transport processes associated with carbon sequestration. Comput. Sci. Eng.
574 16, 22-31.

575 Trebotich, D., Graves, D., 2015. An adaptive finite volume method for the incompressible Navier–
576 Stokes equations in complex geometries, Commun. Appl. Math. Comput. Sc., 10(1), 43–82,
577 doi:10.2140/camcos.2015.10.43.

578 White, A.F., Brantley, S.L., 1995. Chemical Weathering Rates of Silicate Minerals: Reviews in
579 Mineralogy 31, Mineralogical Society of America, Washington, D.C.

580 Wolery, T.J., and Daveler, S.A., 1992. EQ3/6: A software package for geochemical modelling of
581 aqueous systems: Package overview and installation guide (version 7.0). Technical Report
582 UCRL-MA-110662 PT I ed. Lawrence Livermore National Laboratory, USA (1992)

Figure(s)

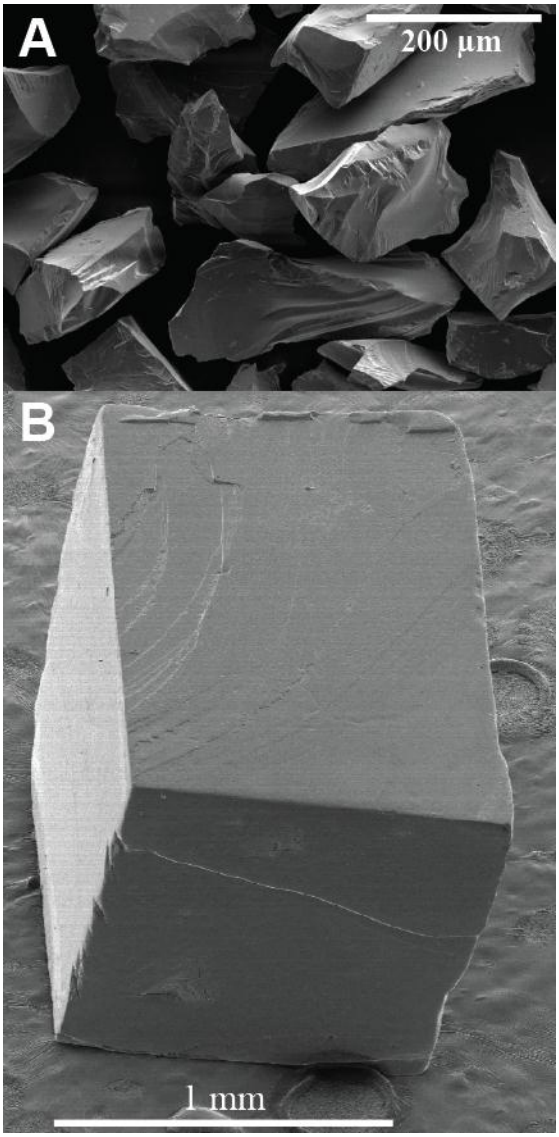

Figure 1: SEM imagery associated with mineral samples used in this study. **A**: forsterite powder used in this study (63 – 150 µm size fraction); **B**: individual calcite rhomb as typically used in this study.

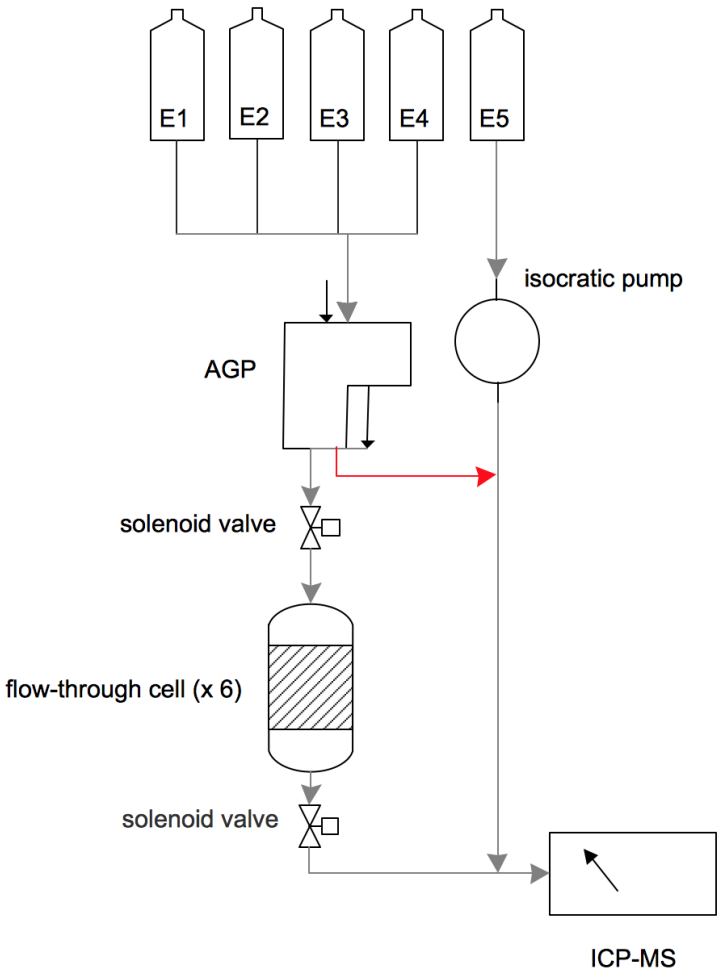

Figure 2: Schematic of the flow-through dissolution module. E1 – E5 represent eluent bottles, where E1 – E4 are used to generate eluents or standards (using an advanced gradient pump, indicted as AGP), and E5 is used to continuously supply an internal standard (here ^{115}In, using an isocratic pump). This flow-through module allows for time-resolved control on incoming eluent composition (here, generating an eluent pH range) by mixing different proportion of DIW with concentrated acid or standard from bottle E1-E4, providing a constant, reproducible flow rate through the flow-through cell, and enabling time-resolved analysis of the effluent stream. A total of 6 flow-through cell positions are available by using 2 parallel computer-controlled solenoid valves, allowing for efficiently measuring blanks and multiple samples. When running standards, the solenoid valve holding the flow-through cells is bypassed, as indicated in red.

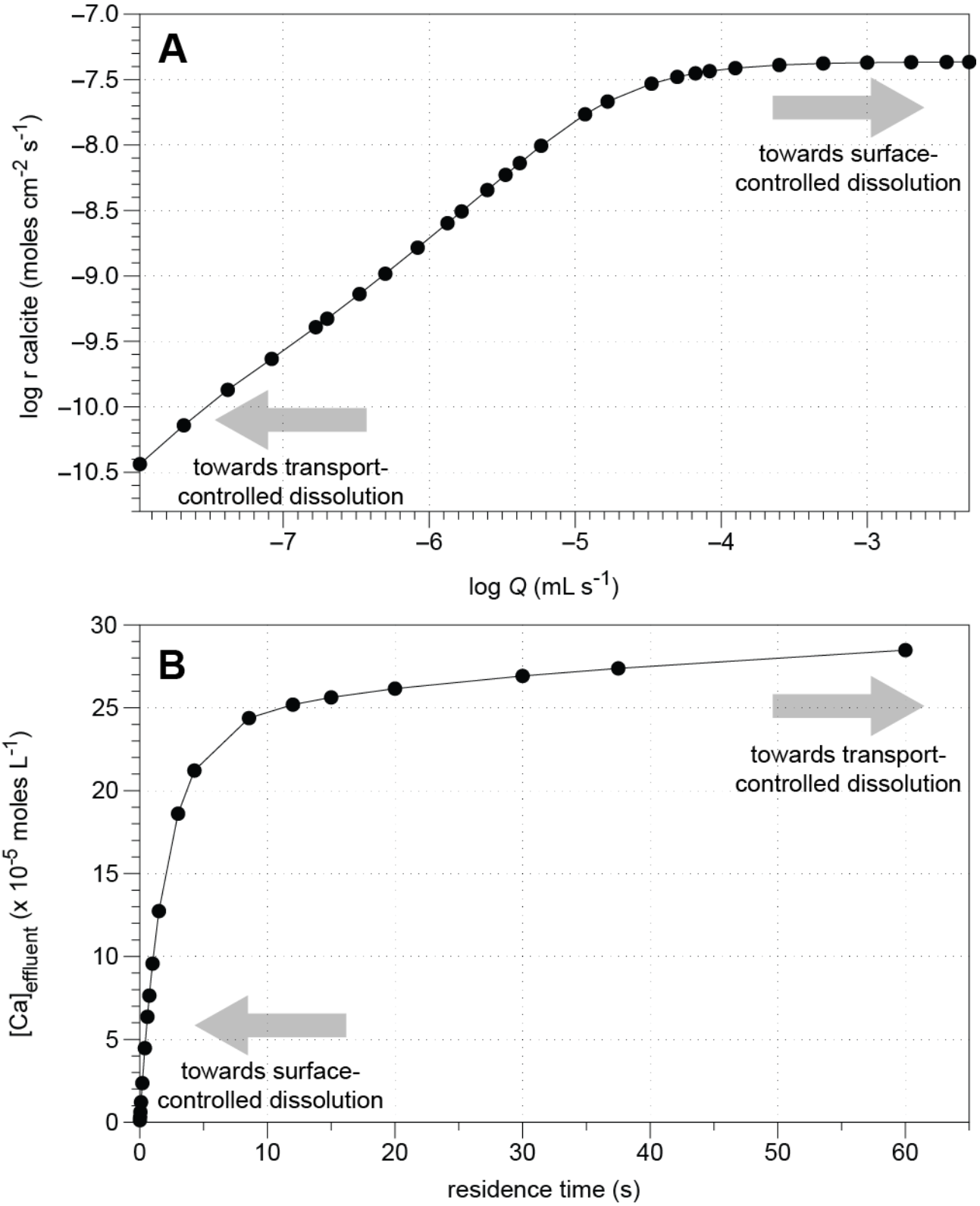

Figure 3: Conceptual representation of proposed FT-TRA approach to assess dissolution regime. If mineral dissolution is approaching surface-controlled conditions, dissolution rates remain constant under varying flow rates (Panel **A**, under relatively fast eluent flow rates) and the steady-state effluent reaction product species concentration (here: [Ca]) increases

proportionally with eluent residence time (Panel **B**, at relatively short eluent residence times). In contrast, if dissolution rates vary with the flow rate (Panel **A**, under relatively slow eluent flow rates), transport processes are affecting the rate of dissolution. Under these conditions, steady-state dissolved species concentration will deviate from linearity with eluent residence time (Panel **B**, at relatively long eluent residence times), and eventually plateau to equilibrium conditions ($C_{surface} = C_{saturation}$). Data shown here were obtained using equivalent 1-dimensional continuum-scale simulations of a grain of calcite of approximately the same size as those in the FT-TRA cell exposed to a solution at pH = 3.3 under a range of eluent flow rates. Because the continuum model – in contrast with the pore scale model – assumes well-mixed conditions within each grid cell of the domain, it can simulate the two end-members of the dissolution regime continuum, i.e. surface-controlled ($C_{surface} = C_{bulk}$) and transport-controlled ($C_{surface} = C_{saturation}$) conditions, providing a convenient way to illustrate the proposed FT-TRA approach to determine the prevalent dissolution regime.

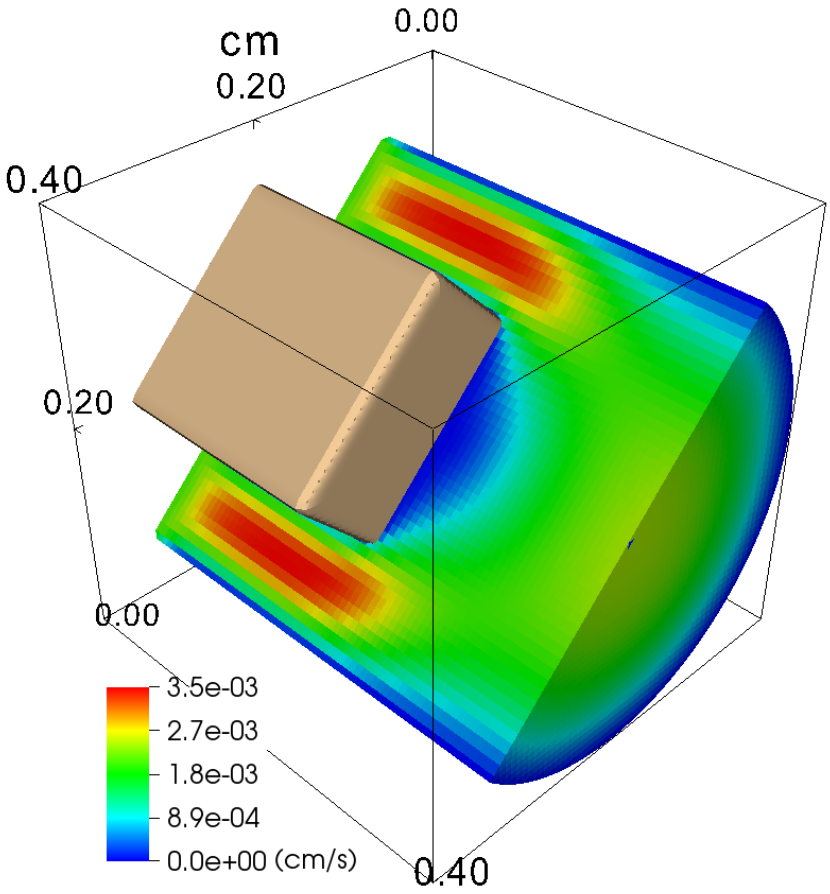

Figure 4: Pore-scale simulation domain showing the calcite grain placed at the inlet end of the reactor. Contours of the magnitude of the fluid velocity in the reactor are shown on a slice that divides the domain in half. Fluid flows from left to right at the slowest experimental rate used (1.67×10^{-4} mL s^{-1}), which is prescribed using a uniform fluid velocity distribution at the inlet face.

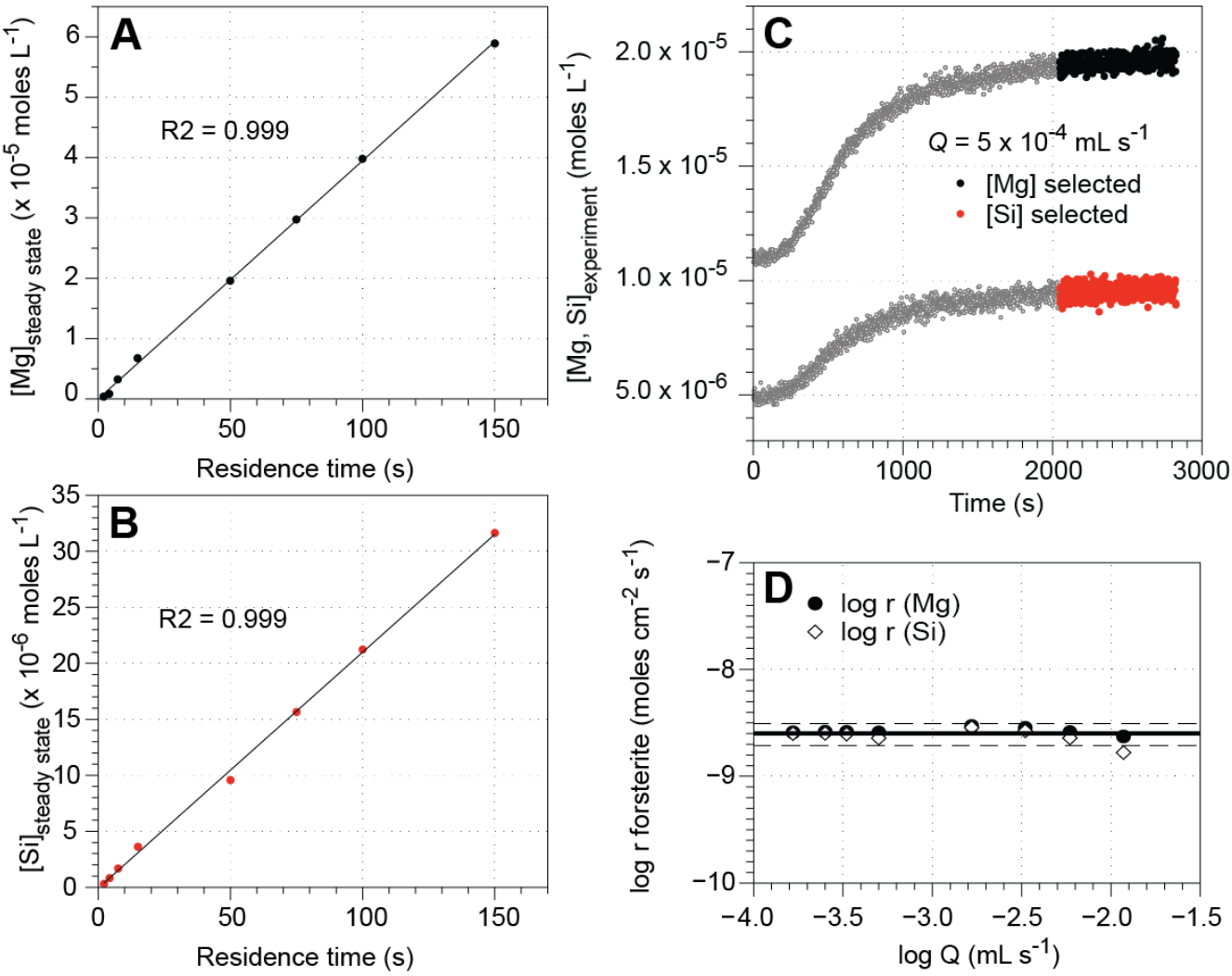

Figure 5: Panels **A** and **B** show $[Mg]_{steady\ state}$ and $[Si]_{steady\ state}$ concentrations respectively (calculated using average $[Mg, Si]_{selected}$ obtained from applicable data as illustrated using data collected as shown in Panel **C**); error falls within symbol size; $R^2 = 0.999$ for both [Mg] as well as [Si] versus eluent residence time. Panel **C**: Time-resolved [Mg, Si] concentration results collected at an eluent flow rate of $5 \times 10^{-4}\ mL\ s^{-1}$ at eluent pH 2.3 illustrates data that is typically collected measured during forsterite powder dissolution experiments. Selected [Mg, Si] concentrations representing steady-state conditions are shown as black filled circles for Mg and red filled circles for Si. Data recorded prior to $[Mg, Si]_{selected}$ plateaus are shown as grey circles. Panel **D**: BET surface area normalized Mg and Si based forsterite dissolution rates versus eluent flow rate (note logarithmic x- and y-axis). $[Mg]_{selected}$ concentrations were divided by 1.81 to take into account forsterite stoichiometry. Average dissolution rate shown as solid black line, 95 % CI based on 2σ shown as dotted black line.

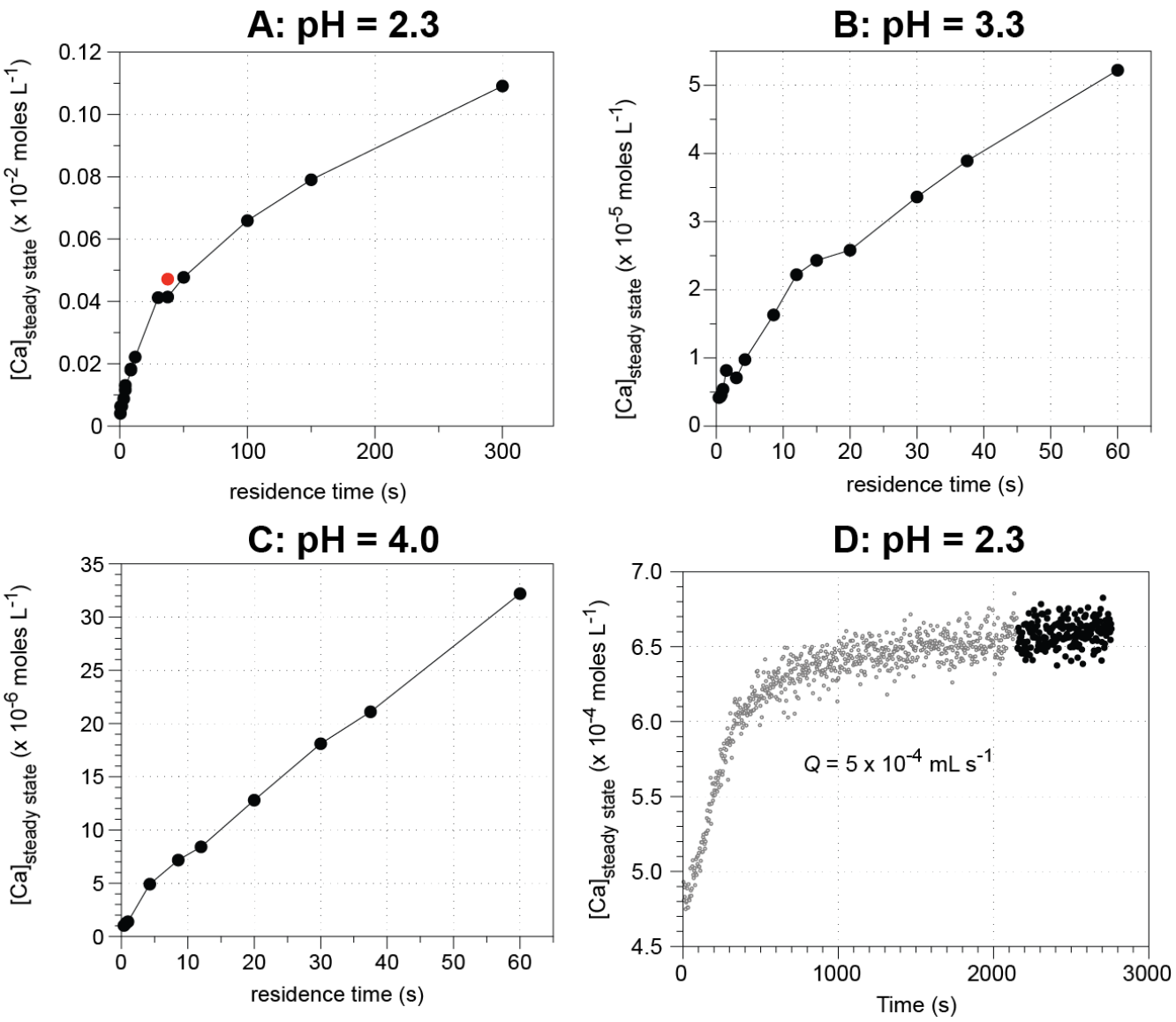

Figure 6: Panels **A**, **B** and **C** show $[Ca]_{steady\ state}$ concentrations collected under eluent pH of 2.3, 3.3 and 4.0 respectively plotted versus eluent residence time. Error falls within symbol size. $[Ca]_{steady\ state}$ concentrations were calculated using average $[Ca]_{selected}$ obtained from applicable data as illustrated using time-resolved data collected at flow rate $Q = 5 \times 10^{-4}\ mL\ s^{-1}$ at eluent pH 2.3 in Panel **D**. Selected [Ca] concentrations representing steady-state conditions are shown as black filled circles.

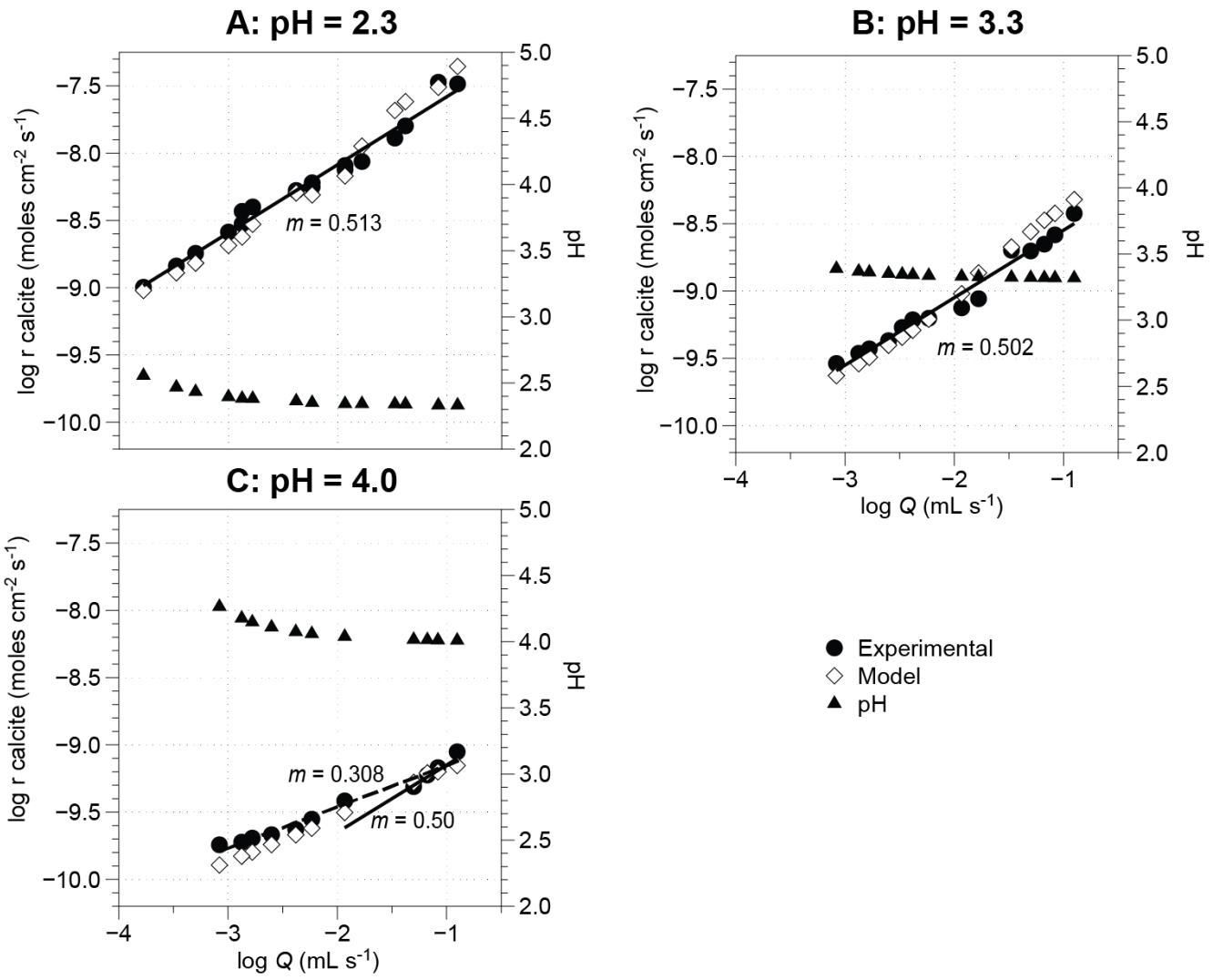

Figure 7: Panels **A**, **B**, **C** show calcite dissolution rates on logarithmic scale from experimental data (black filled circles, error falls within symbol size), and the pore scale modeling (black diamonds) under incoming eluent pH of 2.3, 3.3 and 4.0 respectively. Solid lines in **A** and **B** display linear fit through experimental data. Dashed line in **C** displays linear fit through experimental data. Solid black line in **C** solely shown to represent approximate hypothetical linear fit with a slope of 0.5. Pore scale modeling data were obtained using k_1, k_2 from Chou et al. (1989), and k_3 from Busenberg and Plummer (1986). Modeled effluent pH data is also shown (black filled triangles, axis shown on right).

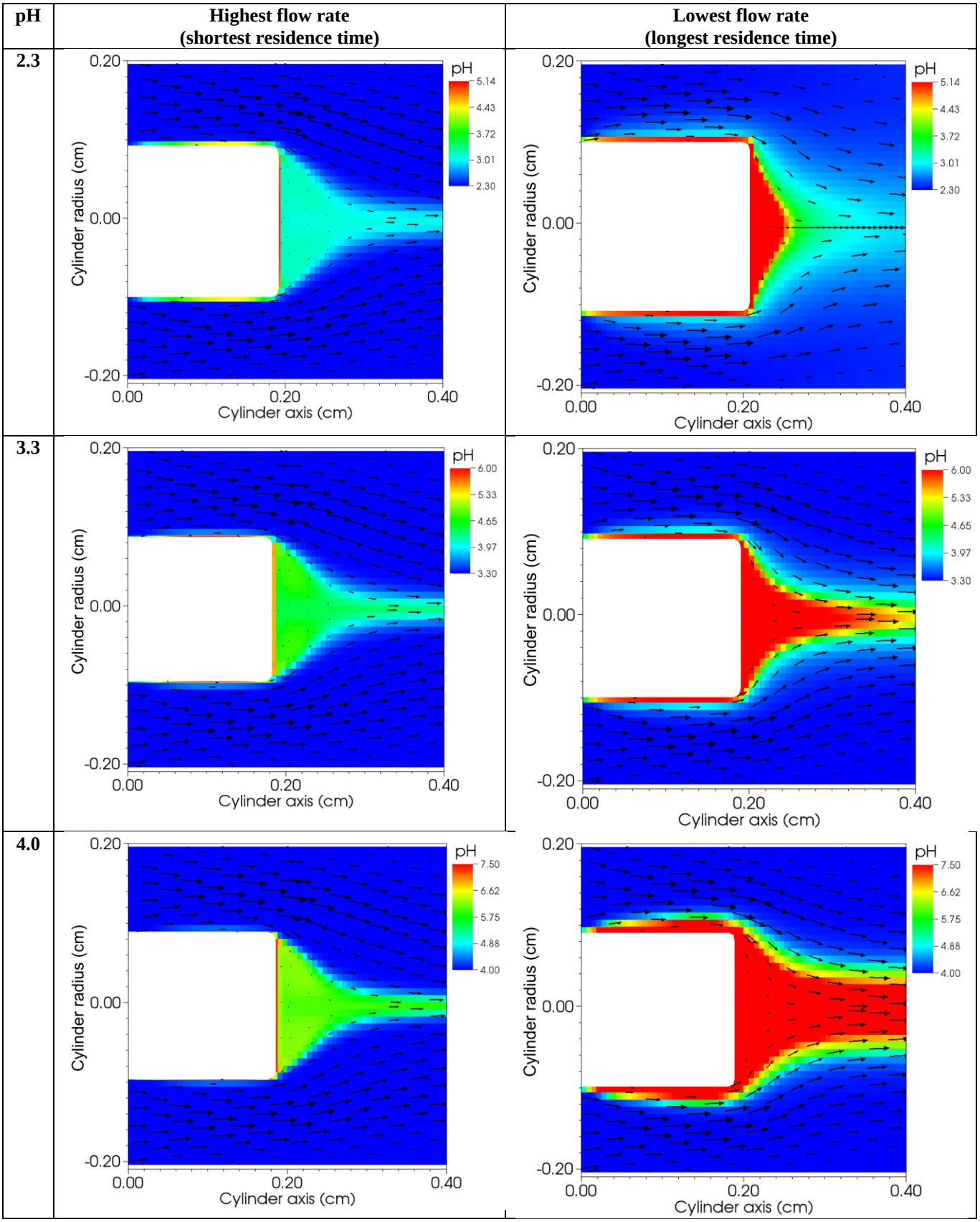

Figure 8: Model domain cross-section (simulations are 3-dimensional), showing transport-controlled calcite rhomb (represented as white square) dissolution during highest left) and lowest (right) flow rate conditions at different incoming

eluent pH conditions (pH = 2.3 at top, pH = 3.3 in middle, pH = 4.0 at bottom). Color gradient within flow-cell indicates pH. Eluent velocity direction and magnitude indicated by arrow direction and length (scaled in each plot), respectively.

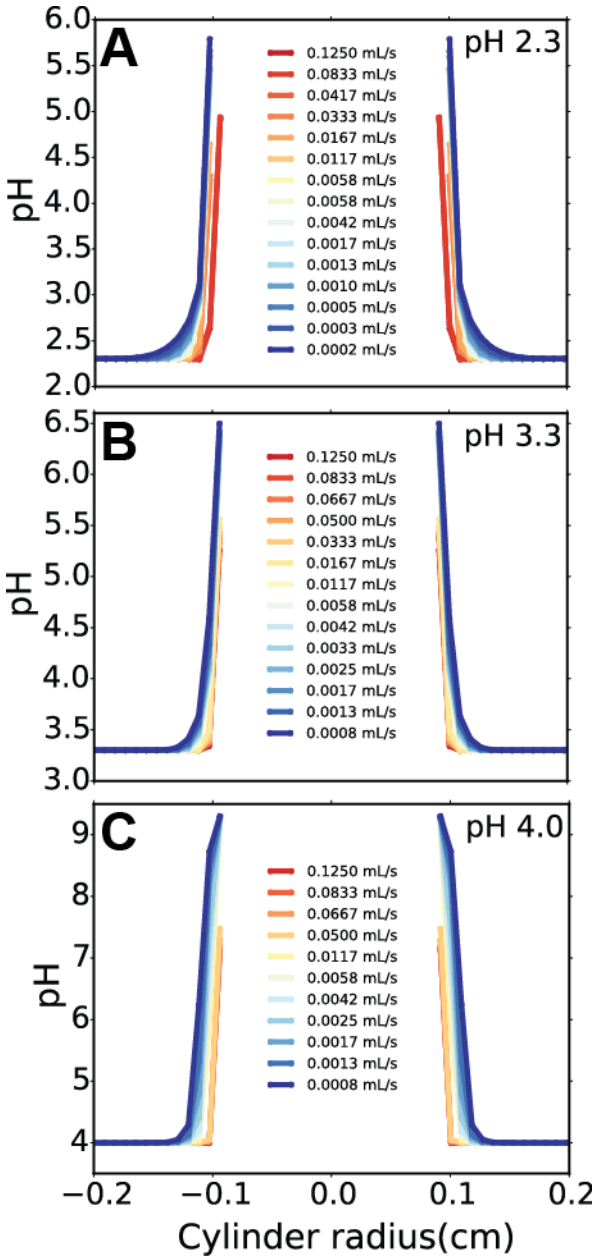

Figure 9: Simulated pH values plotted along the diameter of the cylinder used in the simulation domain, intersecting perpendicularly the mineral grain surface at 0.1 cm from the inlet. Departure from bulk pH at either side of the grain (center blank zone) shows the variation of the DBL thicknesses at 0.1 cm from the inlet face as a function of flow rates (as indicated) at (**A**) eluent pH 2.3, (**B**) eluent pH 3.3 and (**C**) eluent pH 4.0.

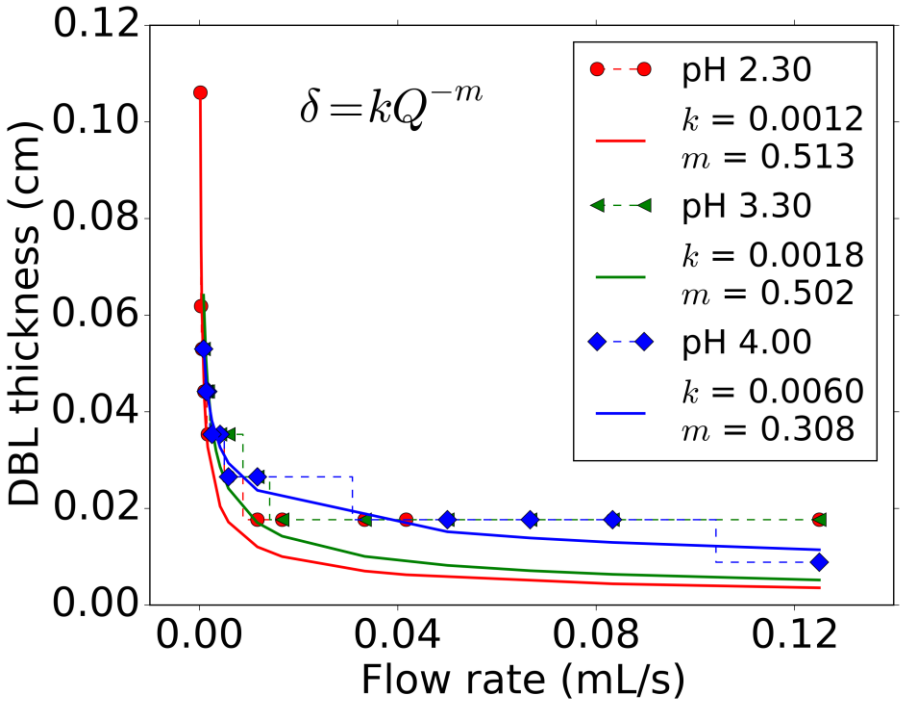

Figure 10: Thickness of the DBL as a function of eluent flow rate. In symbols are DBL thicknesses extracted from Fig. 9 (distance from the point where pH departs from bulk solution value to the point at the mineral surface where pH is highest). Dashed lines indicate the steps corresponding to the grid cells in discretized numerical domain. Solid lines are a fit to simulated DBL thicknesses using the slope *m* obtained in the fit to experimental data (Fig. 7).

Table(s)

Flow rate ($mL\ s^{-1}$)	Forsterite	Calcite		
	pH = 2.3	**pH = 2.3**	**pH = 3.3**	**pH = 4.0**
1.25×10^{-1}		x	x	x
8.33×10^{-2}		x	x	x
6.67×10^{-2}			x	x
5.00×10^{-2}			x	x
4.17×10^{-2}		x		
3.33×10^{-2}		x	x	
1.67×10^{-2}		x	x	
1.17×10^{-2}	x	x (n = 2)	x	x
5.83×10^{-3}	x	x (n = 2)	x	x
4.17×10^{-3}		x	x	x
3.33×10^{-3}	x		x	
2.50×10^{-3}			x	x
1.67×10^{-3}	x	x	x	x
1.33×10^{-3}		x (n = 2)	x	x
1.00×10^{-3}		x		
8.33×10^{-4}			x	x
5.00×10^{-4}	x	x		
3.33×10^{-4}	x	x		
2.50×10^{-4}	x			
1.67×10^{-4}	x	x		

Table 1: Overview of constant incoming eluent pH experiments (indicated in bold) conducted as part of this study. Effluent [Mg, Si] for forsterite and [Ca] concentrations were monitored using time-resolved analysis until steady state dissolution was achieved.

$Aqueous\ reaction\ (secondary\ species \rightleftharpoons reactants)$	$\log K_{eq}$
$OH^- \rightleftharpoons -H^+ + H_2O$	13.9
$HCO_3^- \rightleftharpoons -H^+ + H_2CO_{3\,(aq)}$	6.3
$CO_3^{2-} \rightleftharpoons -2H^+ + H_2CO_{3\,(aq)}$	15.9
$CaCO_3 \rightleftharpoons -2H^+ + H_2CO_{3\,(aq)} + Ca^{2+}$	13.3
$CaHCO_3^+ \rightleftharpoons -H^+ + H_2CO_{3\,(aq)} + Ca^{2+}$	5.3
$CaOH^+ \rightleftharpoons -H^+ + H_2O + Ca^{2+}$	12.8
$HNO_{3\,(aq)} \rightleftharpoons H^+ + NO_3^-$	1.3
$CaNO_3^- \rightleftharpoons NO_3^- + Ca^{2+}$	-1.3

Table 2: List of aqueous complexation reactions and equilibrium constants sourced from the EQ3/6 database (Wolery and Daveler, 1992).